Northumbria Research Link

Northumbria
University
NEWCASTLE

University**Library**

TABLE OF CONTENTS (TOC)

An Active Bacterial Anti-adhesion Strategy Based on Directional Transportation of Bacterial Droplets Driven by Triboelectric Nanogenerators

Jing Lin[1,*], Jialin Li[1], Shichang Feng[1], Caiqin Gu[1,*], Huajian Li[1], Hanqing Lu[1], Fei Hu[1], Duo Pan[2], Ben Bin Xu[3], and Zhanhu Guo[2,*]

[1]School of Chemistry and Chemical Engineering, Guangzhou University, Guangzhou 510006, China

[2] Integrated Composites Laboratory (ICL), Department of Chemical & Biomolecular Engineering, University of Tennessee, Knoxville, TN 37996, USA

[3] Mechanical and Construction Engineering, Faculty of Engineering and Environment, Northumbria University, Newcastle upon Tyne, NE1 8ST, UK

An active bacterial anti-adhesion strategy based on directional transportation of bacterial droplets driven by a triboelectric nanogenerator has been reported.

Provide the authors' webside if possible.

Jing Lin, https://www.x-mol.com/groups/lin_jing

Zhanhu Guo, http://composites.utk.edu/Publications.html

An Active Bacterial Anti-adhesion Strategy Based on Directional Transportation of Bacterial Droplets Driven by Triboelectric Nanogenerators

Jing Lin[1] (✉), Jialin Li[1], Shichang Feng[1], Caiqin Gu[1](✉), Huajian Li[1], Hanqing Lu[1], Fei Hu[1], Duo Pan[2], Ben Bin Xu[3], and Zhanhu Guo[2](✉)

[1] School of Chemistry and Chemical Engineering, Guangzhou University, Guangzhou 510006, P. R. China

[2] Integrated Composites Laboratory (ICL), Department of Chemical & Biomolecular Engineering, University of Tennessee, Knoxville, TN 37996, USA

[3] Mechanical and Construction Engineering, Faculty of Engineering and Environment, Northumbria University, Newcastle upon Tyne, NE1 8ST, UK
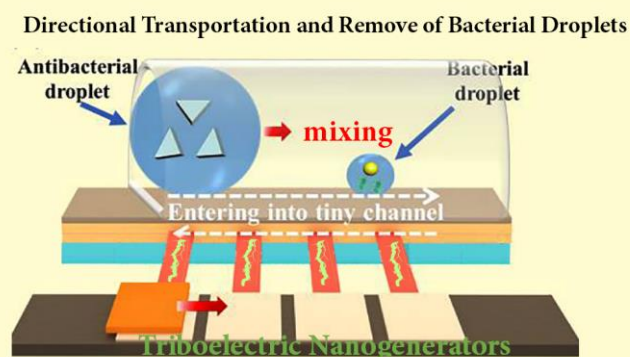
ABSTRACT

An active bacterial anti-adhesion strategy based on directional transportation of bacterial droplets driven by a triboelectric nanogenerator (TENG) has not been reported to date, although passive defense approaches can prevent bacterial adhesion by regulating superwetting surfaces combined with incorporated antibacterial substances. Here a triboelectric nanogenerator driving droplet system (TNDDS) was built to drive directional transportation of bacterial droplets to be eliminated, which comprises TENG with periodical frictional Kapton film and aluminum foils and a superhydrophobic driving platform (SDP) with paralleled driving electrodes. The current generated by the TENG triboelectricity is transmitted to the paralleled driving electrodes to form an electric field driving the directional transportation of charged droplets. The critical value of the driven droplet volume on SDP is closely related to the distributed electrodes' distance and width, and the driving distance of droplets is related to the number of electrodes. More crucially, TNDDS can actively drive the charged droplets of prepared triangular silver nanoprisms (Ag NPs) forward and back to mix with and remove a tiny bacterial droplet on an open SDP or in a tiny semi-enclosed channel. Bacteria could be killed by releasing Ag+ and effectively removed by TNDDS by regulating the motion direction. Generally, this approach offers a promising application for removing bacteria from material surfaces driven by TENG and opens a new avenue for bacterial anti-adhesion.

1 Introduction

It has been inferred that there exist around 10^{31} bacteria on the earth, harmful bacteria can spread and adhere to the human body surface and then invade human cells from the outside to the inside to destroy the body and take countless innocent lives [1]. Bacteria can also adhere to the surface of different materials through their characteristics and further breed and form robust biofilms[2]. Biofilms can cause the spread of pathogenic bacteria, microbial contamination, and material surface corrosion, which will bring bacterial infected risk to food packaging, medical fabric, biosensor, biomedical equipment, and microbial corrosion loss to industrial pipelines, marine ships, and engineering materials, etc[3-5]. Several studies have shown that a feasible scientific approach to hinder

Address correspondence to Jing Lin, linjin00112043@126.com; Caiqin Gu, gcq86@163.com; Zhanhu Guo, nanomaterials2000@gmail.com;

the harm of bacteria and microorganisms is to develop various bacterial anti-adhesive surfaces to prevent the initial adhesion of bacteria and the formation of bacterial biofilm. Thus, it is of great research significance for human health and the global economy to develop some cutting-edge technologies of bacterial anti-adhesion[6, 7].

Recently, numerous studies have been conducted by scientists at home and abroad to continuously inhibit and reduce the adhesion of bacteria at the initial stage, and thus eliminate and cut off the breeding of bacteria on the surface[8, 9]. The design idea of repelling or blocking bacteria has been used to construct superhydrophobic or superhydrophilic surfaces to reduce bacterial adhesion. An approach is to construct a superhydrophobic surface with micro/nanostructure and low surface energy. The interspaces' air layer in the micro/nano structure on the superhydrophobic surface in a Cassie state is conducive to preventing the adhesion of bacterial droplets[10, 11]. For instance, Doris Vollmer's team[12] designed a polyurethane microfluidic tube with an inner diameter of 1 cm, which was oxidized by Fenton solution to form a layer of nanofilaments, and then modified with methyl trichlorosilane or tetraethoxysilane and 1H,1H,2H,2H-perfluorodecyltrichlorosilane to make it superhydrophobic. After the bacterial anti-adhesion experiment, the bacteria that adhered to the superhydrophobic microfluidic tube were reduced by more than 20 times than that of the unmodified one. This exceptional resistance to bacterial contamination is due to the characteristic spacing of its irregular 3D nanofilaments, which are just smaller than the size of *E. coli* and prevents bacteria from entering the pores. Furthermore, inspired by the self-cleaning effect of superhydrophobic lotus leaf, Limei Tian [13] et al. prepared a regular array structure composed of vertically arranged micro-scale silicon cylinder and nanoscale ZnO nanoneedle. A superhydrophobic surface with outstanding bacterial anti-adhesion and mechanical sterilization performance was obtained after treatment with fluorosilane, and its bacterial anti-adhesion rate reached 99%. This bacteria-repellent performance is primarily due to the presence of a stable Cassie state on the superhydrophobic surface, which can significantly reduce the contact area of the liquid-solid interface and thus reduce bacterial adhesion[14-16]. Additionally, our group further proposed that superhydrophobicity/ superoleophobicity underwater is the underlying mechanism of surface resistance to bacterial adhesion [17, 18]. Another approach is to isolate bacteria; the superhydrophilic surface

was constructed by modifying with hydrophilic polymers or zwitterionic molecules to achieve bacterial anti-adhesion. Superhydrophilic surface in the water environment can rapidly form a hydrated layer because of the strong hydrogen bonding interaction, its large exclusion hinders the bacteria from reaching the surface, and its large hydration repulsion hinders the contact between bacteria and the surface. It is difficult for bacteria to adhere to the hydrophilic surface because they must overcome a certain energy barrier to compress the hydrated molecular layer. The stereoscopic exclusion and hydration effects of hydrophilic surfaces provide them with exceptional resistance to bacterial adhesion [19, 20]. Zhang [21] et al. developed an amphiphilic (PNMBH-PDMS) copolymer coating, the incorporated hydrophilic polyvinylpyrrolidone (PVP) could cause a chain segment migration to the coating surface and form a hydration layer to prevent biofouling (containing proteins, bacteria, and diatoms). Compared with the pristine PDMS coating, PNMBH-PDMS coatings could reduce 82% adhesion of fibrinogen, 97% adhesion of *S. aureus*, and 97% adhesion of diatom. Mei [22] et al. designed a broad-spectrum anti-biofilm coating based on hydrophilic poly(N,N-dimethylacrylamide) polymer, which showed outstanding anti-protein contamination and anti-biofilm adhesion. Our group constructed poly(ethylene glycol) methyl ether methacrylate-containing hydrophilic surfaces, which can achieve different wettability and bacterial anti-adhesion regulation, and first elaborated the underlying mechanism of the hydration layer on bacterial anti-adhesion of the hydrophilic surface through molecular simulation[18]. Although significant progress has been made in superhydrophobic and superhydrophilic-type bacterial anti-adhesion approaches, these two approaches are static and passive. A sole superhydrophobic surface must be inclined to a certain angle so that bacterial droplets can roll off, and a sole superhydrophilic surface has poor durability against bacterial adhesion, so these passive bacterial anti-adhesion approaches limit their application[23].

TENG has become an emerging technology and has attracted extensive attention since it was invented in 2012[24], and it can convert different sources into electric energy, such as wind[25, 26], vibration[27, 28], water flow[29, 30], body movement[31, 32], to power the electronic equipment[33, 34]. More crucially, TENG, based on the coupling effect of contact charging and electrostatic induction, can overcome the low output limitations of conventional piezoelectric generators and offers unique advantages, such as large output power, high

efficiency, low material cost, lightweight, facile manufacturing[35], and has numerous applications in the fields of tunable optical devices[36, 37] and wearable electronic devices[38, 39]. Here, TENG is extended to our work driving charged droplets to realize bacterial anti-adhesion, an active bacterial anti-adhesion strategy based on TNDDS was proposed to drive the directional transportation of bacterial droplets to be removed. **Fig. 1** shows a schematic of the preparation process of TNDDS, which consists of SDP of electric field driving function and TENG with triboelectricity function; droplet driving can be realized due to an exerted electric field by paralleled copper electrodes; to reduce charge loss, an insulating Polytetrafluoroethylene (PTFE) film is pasted on them, and modified with hydrophobic silica particles to reduce the frictional resistance of droplets on the SDP surface; paralleled copper electrodes must be connected with TENG to obtain current generated by TENG triboelectricity. The TENG is a core system for generating electrical currents and is composed of two core parts; an acrylic sheet serves as a fixed plate, where rectangular aluminum foils with a certain distance adhere on the upper surface of the fixed plate, and a Kapton film that adhered on the lower surface of a movable acrylic sheet is driven periodically by a numerical controllable linear motor. To realize driving bacterial droplets' directional transportation, periodical friction occurring on the inner surfaces of the Kapton film with the first aluminum foil to the last layer must be performed, resulting in the generation of an output charge and current. The generated charges are further conducted on the paralleled copper electrodes to generate an electric field driving the directional motion of charged droplets from left to right. Since small bacterial droplets are in narrow areas, in reality, droplet-containing antibacterial agents can be transported to mix with this type of tiny bacterial droplet and were driven back away from this narrow area (e.g., a tiny semi-enclosed channel in our study). Thus, our proposed active bacterial anti-adhesion approach by directional transportation of bacterial droplets driven by the TENG has broad development potential[40, 41].
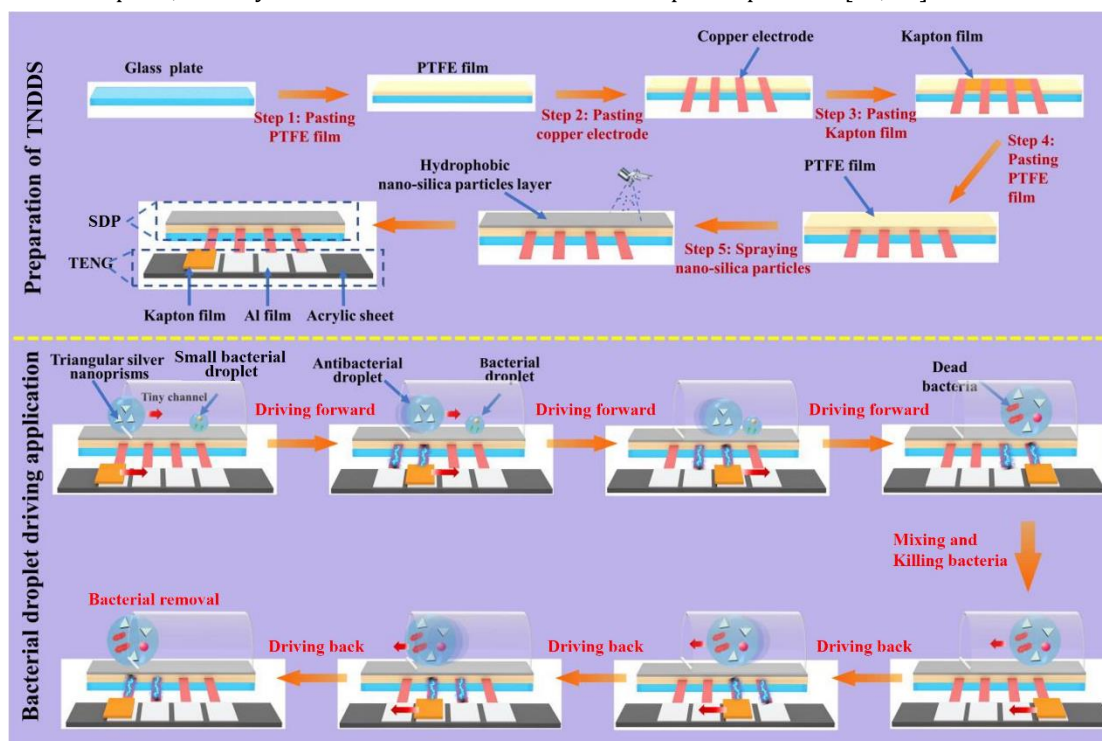
Figure 1 Schematic of the preparation process (**a**) and its bacterial droplet driving application (**b**) of TNDDS comprising TENG and SDP.

2 Experimental

2.1 Materials

Kapton film (Polyimide), PTFE film, copper tape, aluminum foil, and acrylic sheet were purchased from the local market. Anhydrous ethanol (C_2H_6O, 99.5%), hydrophobic SiO_2, silver nitrate ($AgNO_3$, ≥ 99.8%), sodium citrate ($C_6H_5Na_3O_7$, ≥98%), polyvinylpyrrolidone (PVP, MW = 40000 mol g^{-1}), hydrogen peroxide (H_2O_2, 30%), sodium borohydride ($NaBH_4$, ≥98%) were purchased from Shanghai Macklin Biochemical Co., Ltd. Shanghai Luwei Microbial Sci. & Tech. Co., Ltd. Supplied the *staphylococcus aureus* (CMCC(B) 26003)(*S.aureus*) and *Escherichia coli* (CMCC(B) 44102)(*E. coli*). Sigma Aldrich supplied phosphate-buffered saline (PBS), Mueller-Hinton agar (MHA), and Mueller-Hinton broth (MHB). Invitrogen (Carlsbad, CA, USA) supplied the LIVE/DEAD Backlight bacterial viability kit (SYTO9/PI). A numerically controlled linear motor was

purchased from a local market. A Keithley 6514 System Electrometer, high voltage probe (P5122), and an oscilloscope (MD032(3-BW-200) were purchased from Teck (China) Technology Co., LTD.

2.2 Inductively coupled plasma etching modification of Kapton film

Kapton thin film with a nanopatterned surface was prepared by inductively coupled plasma (ICP) reactive-ion etching. A 50 μm of Kapton film was sequentially cleaned with methanol, isopropyl alcohol, and deionized water, and then dried by blowing nitrogen gas. Subsequently, at flow rates of 10, 20, and 30 sccm, the ICP chamber was injected with Ar, O_2, and CF_4 gases, respectively. The nanopatterned structure was obtained on the Kapton film surface by ICP reactive-ion etching for 15 min (plasma-ion acceleration = 100 W) [42].

2.3 Preparation of TENG

The TENG was designed with two core parts (a fixed and a movable one). As illustrated in Fig. 1, for the fixed part, an acrylic sheet (40 cm×8 cm) is served as a fixed supporting substrate at the bottom, where rectangular aluminum foils (10 cm×8 cm×25 μm) with a certain distance of 1 cm adhere on the upper surface of fixed acrylic sheet. For the movable part, Kapton film that adhered to the lower surface of a movable acrylic sheet is driven periodically by a numerical controllable linear motor; the above two fabricated plates are kept in parallel with each other, where the inner surfaces (Kapton film and aluminum foils) are in intimate contact, and their periodical friction generates output to charge and current.

2.4 Preparation of SDP

First, the glass slides were alternately ultrasonicated thrice in water and anhydrous ethanol for 10 min in an ultrasonic cleaning machine to clean the oil stains and impurities on the glass surface. Second, a PTFE film with a thickness of 80 μm was pasted on the glass slide for insulation, and then parallel copper strip tapes of a given size were pasted on the PTFE film as driving electrodes. Third, another PTFE film covered the copper electrodes protecting them from voltage breakdown. To reduce the frictional force of droplet directional transportation on SDP, the top PTFE film was further sprayed with 0.05 mg hydrophobic silica in ethanol dispersion (0.125 wt%) on a heating plate of 80°C and dried in an oven at 80°C for 1 min.

2.5 Preparation of the TNDDS

The TNDDS was constructed by assembling the obtained TENG and SDP by connecting the driving electrodes and aluminum foils with alligator clip wires.

2.6 Synthesis of Ag NPs

Ag NPs were synthesized by the reduction approach based on the previously reported literature[43]. Typically, 25 mL of 0.1 mM $AgNO_3$ solution was poured into a beaker on a magnetic stirrer, 1.5 mL 30 mmol/L $Na_3C_6H_5O_7$ and 1.5 mL 0.7 mM PVP solutions were successively taken by a pipette gun into the above solution. Magnetic force stirred the solution for 2–3 min, making it uniform. 60 μL 30% H_2O_2 was then added to the mixture with a pipette gun and stirred with magnetic force again for 10 min. After that, 140 mL of 100 mM $NaBH_4$ solution was injected into the above mixture. The solution changed from light yellow and dark blue to final sky blue after 40 min of reaction.

2.7 Droplets directional transportation for bacterial removal driven by a triboelectric nanogenerator

Water and bacterial droplets directional transportation is performed using TNDDS, to simulate the removal of small bacterial droplets in narrow areas, in reality, 5 μL small bacterial droplet was added in a tiny semi-enclosed channel on SDP, and then 100 μL Ag NPs droplet was added to SDP using a pipetting gun. The Ag NPs droplet was driven into the tiny channel by the TENG with a linear reciprocating motor directional at a speed of 18 cm/s so that the Ag NPs droplet was mixed with the small bacterial droplet in the tiny channel. Finally, the mixed droplets are driven to remove away from the tiny channel by performing the reverse motion of the linear reciprocating motor.

2.8 Antibacterial activity tests

The antibacterial activities of Ag NPs with various concentrations were evaluated by measuring their antibacterial rate. Typical bacterial microorganisms, including *S. aureus* and *E. coli*, were selected for experimental assessment. The obtained Ag NPs solution was diluted to 0.2, 0.4, 0.6, 0.8, and 1.0 mg/mL. Each sterile test tube was charged with 1 mL Ag NPs suspension and 1 mL bacterial suspension containing 10^7 colony units (CFU), controls (without Ag NPs) were also performed with 1 mL of sterile water substituting Ag NPs. Then, at 37°C and 150 rpm for 15 h, the testing tubes were incubated with a shaking incubator. 1 mL bacterial solution was taken out from the tubes and charged into another testing tube containing 9 mL PBS after the oscillating incubation and was diluted by a certain multiple. 100 μL diluent was taken out and inoculated uniformly onto the surface of solidified MHB plates

in sterilized Petri dishes, and then incubated at 37°C for 24 h. After counting the number of colonies, the number of bacteria was computed by multiplying the dilution factor, and the antibacterial rate was computed using the following Eq. (1):

Antibacterial rate (%) = (CFU$_{control}$ mL^{-1}−CFU$_{sample}$ mL^{-1})/CFU$_{control}$ mL^{-1} (1)

where CFU$_{control}$ mL^{-1} is the average number of bacteria for the control and CFU$_{sample}$ mL^{-1} is the average number of bacteria for Ag NPs samples. Besides assessing the antibacterial rate, live/dead bacterial viability assays were used to intuitively evaluate the antibacterial activities of Ag NPs samples after the above oscillating incubation, which is dual fluorescence staining approach using the fluorescent dyes of SYTO9/propidium iodide (PI), SYTO9 binds DNA and RNA, emitting green fluorescence, PI only permeates dead or damaged cells, emitting a red fluorescence. 100 μL bacterial suspension was applied to a piece of the sterilized glass slide, 25 μL fresh SYTO9/PI mixture was added to the surface of bacteria using a microliter syringe, and then was covered with a piece of the glass coverslip, the bacterial thoroughly staining was performed at room temperature in darkness for 15 min. Afterward, the live/dead bacterial state was observed under an Olympus BX51 epifluorescence microscope employing green and red filters with excitation/emission 440–480 nm/515–540 nm and 540–560 nm/630–660 nm, respectively. The bactericidal efficacy of the mixed droplets after Ag NPs droplet was mixed with the bacterial droplet was also examined, after performing droplets directional transportation for bacterial removal (Part 2.7), the mixed droplet was transferred into a centrifuge tube for incubation at 37°C for 15 h. The mixed droplet is then dissolved in 9.9 mL PBS with 100 times dilution. Finally, 100 μL diluent was taken out and inoculated uniformly onto the surface of the solidified MHA plate in a sterilized Petri dish, the subsequent incubation process and the computation of antibacterial rate was the same as above.

2.9 Bacterial anti-adhesion assessment

The optimal SDP with the best superhydrophobicity and lowest adhesive force was selected to test its bacterial anti-adhesion. *S.aureus* was used as the representative of gram-positive bacteria and *E. coli* as the representative of gram-negative bacteria. 100 μL bacterial droplets with 10^7 colony units (CFU) were placed on the SDP surface for 4 h and then transferred into a sterilized centrifuge tube, 10 sml sterile PBS solution was used to rinse the SDP surface to add to the centrifuge tube. The

obtained bacterial solution was diluted with sterilized water for 1000-fold dilution; 100 μL diluent was taken out and inoculated uniformly onto the surface of the solidified MHA plate in a Petri dish, and then incubated at 37°C for 24 h. A 100 μL bacterial droplet with 10^7 colony units (CFU) was taken for control after incubation. The bacterial anti-adhesion rate (R, %) of the SDP surface is computed using Eq. (2):

R=(CFU$_{sample}$mL^{-1}/CFU$_{control}$mL^{-1})×100% (2)

where CFU$_{sample}$ mL^{-1} is the mean value of bacterial colonies in the experimental groups repeated thrice, CFU$_{control}$ mL^{-1} is the mean value of bacterial colonies in the control groups repeated thrice.

2.10 Characterization methods

A field emission scanning electron microscope (Zeiss Sigma 300, Zeiss, Germany) was used to observe the surface morphologies of the Kapton film and SDP; the surface roughness of the Kapton film was tested employing an atomic force microscope (Bruker Dimension ICON, Bruker, USA). The elements' distribution was examined using X-ray photoelectron spectroscopy (XPS, K-Alpha+, Thermo Fisher Scientific, American) with an energy dispersive spectrometer (EDS, Smartedx, Zeiss, Germany). Water contact angles, the rolling angle, advancing angle, receding of the water droplet, and contact angle hysteresis was measured using a contact angle meter (OCA40 Micro, Data physics, Germany). The adhesion forces of a water droplet on an SDP surface were measured using a high-sensitive microelectromechanical balance system (Data-Physics DCAT11, Germany). Characteristic absorption peaks of triangular Ag NPs were measured by UV–Vis spectrophotometer (Shimadzu UV-1800, Japan). The micromorphology of triangular Ag NPs was observed using transmission electron microscopy (Philips EM 301 TEM). Samples were prepared by dropping an Ag NPs solution on carbon-coated copper grids.

2.11 Output performance test of TENG

Removable Kapton film adhered to an acrylic sheet fixed on the sliding platform of a numerically controlled linear motor; several aluminum foil friction electrodes were placed on an acrylic sheet fixed on a lifting platform; the height of the lifting platform was adjusted so that the Kapton film's inner surface was in close contact with a fixed aluminum foil friction electrodes and placed on the sliding platform of the linear motor with periodic reciprocating movement at a speed of 18 cm/s. The fixed aluminum foil friction electrode was connected

to a Keithley 6514 high precision electrometer to output the short circuit current of the TENG by the reciprocating motion of the Kapton film driven by a linear motor. A fixed aluminum foil friction electrode is connected to a high voltage probe and oscilloscope to output its open circuit voltage.

3 Results and discussion

3.1 Characterization and performance of the triboelectric nanogenerator

To increase the loaded charge density on the Kapton film's surface and enhance the triboelectric performance of the TENG, ICP was performed on the Kapton film to increase its triboelectric performance[44]. The Kapton film's surface before etching shows that its surface morphology is relatively smooth ((**Fig. 2(a)**), after etching, a nanoscale structure is formed on the surface of the Kapton film ((**Fig. 2(b)**). The surface roughness of Kapton film after ICP etching significantly increases from 0.932 nm **(Fig. 2c)** to 25.1 nm **(Fig. 2d)**. The Kapton film's reciprocating movement is driven by a motor, and the horizontal reciprocating friction between the Kapton film and aluminum foil electrode plate in close contact generates open circuit voltage (**Fig. 2(e)**) and short circuit current (**Fig. 2(f)**). The stable reciprocating speed of the sliding platform and uniform distribution of the nano-patterns etched on the surface of the Kapton film makes the electrical signals generated by the TENG appear stable waveforms, and the maximum peaks of open circuit voltage and short circuit current are 465.2 V and 1.07 μA, respectively[45].

Figure 2 Surface morphologies of the Kapton film before ICP etching (**a**), and after ICP etching (**b**); Surface roughness of Kapton film before ICP etching (**c**),
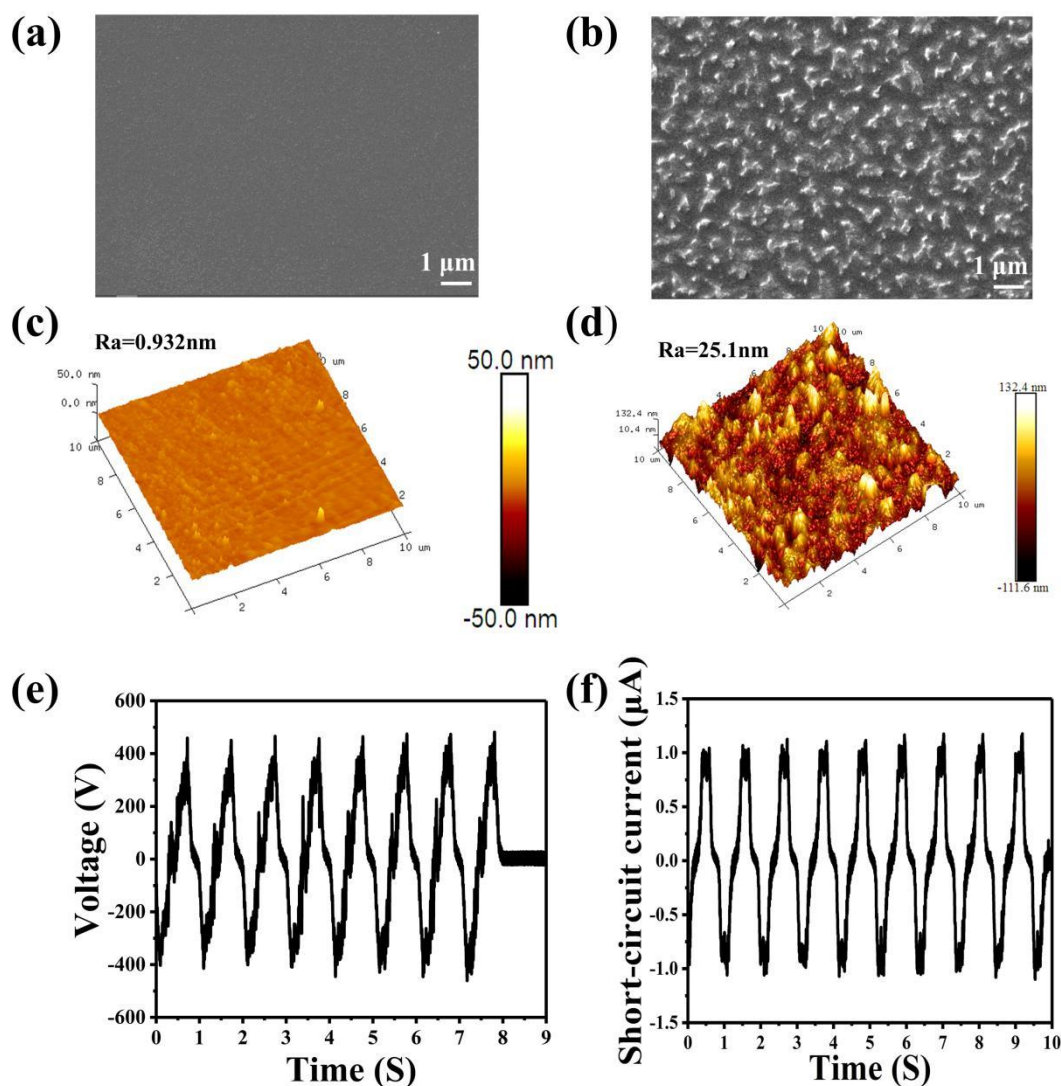
and after ICP etching (**d**); Open circuit voltage (**e**) and short circuit current (**f**) are generated by the TENG.

3.2 Optimization of SDP

<mark>It is crucial to optimize the spraying amounts of hydrophobic silica to reduce the adhesion force of charged droplets on SDP.</mark> The static contact angle, rolling angle, advancing angle, receding angle, contact angle hysteresis, and adhesion force of the droplets on the surface of SDP were examined by varying the sprayed amount of hydrophobic silica (0.35, 0.40, 0.45, 0.5, and 0.55 mg/cm²). The results indicate that, with the increase in sprayed hydrophobic silica amount, the static water contact angle of droplets on the superhydrophobic SDP surface gradually increases from 124.992° to 151.276° (**Fig. 3(a)**), and the rolling angles gradually decrease from 65° to 6° (**(Fig. 3(b)**), and its rolling process is recorded in **Figure S1** in the ESM. Both advancing and receding angles of droplets also get progressively larger from 144° and 122° to 162° and 152°, respectively, as the number of silica increases from 0.35 and 0.55 mg/cm², as illustrated in **Fig. 3(c)**. The corresponding contact angle hysteresis gradually decreases from 22° to 6° (**(Fig. 3(d)**), indicating that the frictional resistance of water droplets on the superhydrophobic SDP surface decreases with the increase in spraying amount, which is more favorable for droplets' directional transportation. **Fig. 3e** the adhesive force measurement setup. **Fig. 3f-j** shows that the adhesive forces of water droplets on the horizontal superhydrophobic SDP surface gradually decrease with the increase in spraying amount. The adhesive force reaches the minimum (0.0501 mN). The adhesive forces of water droplets on SDP surfaces with various spraying amounts was shown in **Figure S2** in the ESM. The spray amount of hydrophobic silica of 0.55 mg/cm² is optimized as the most suitable one on SDP surface[46-48].
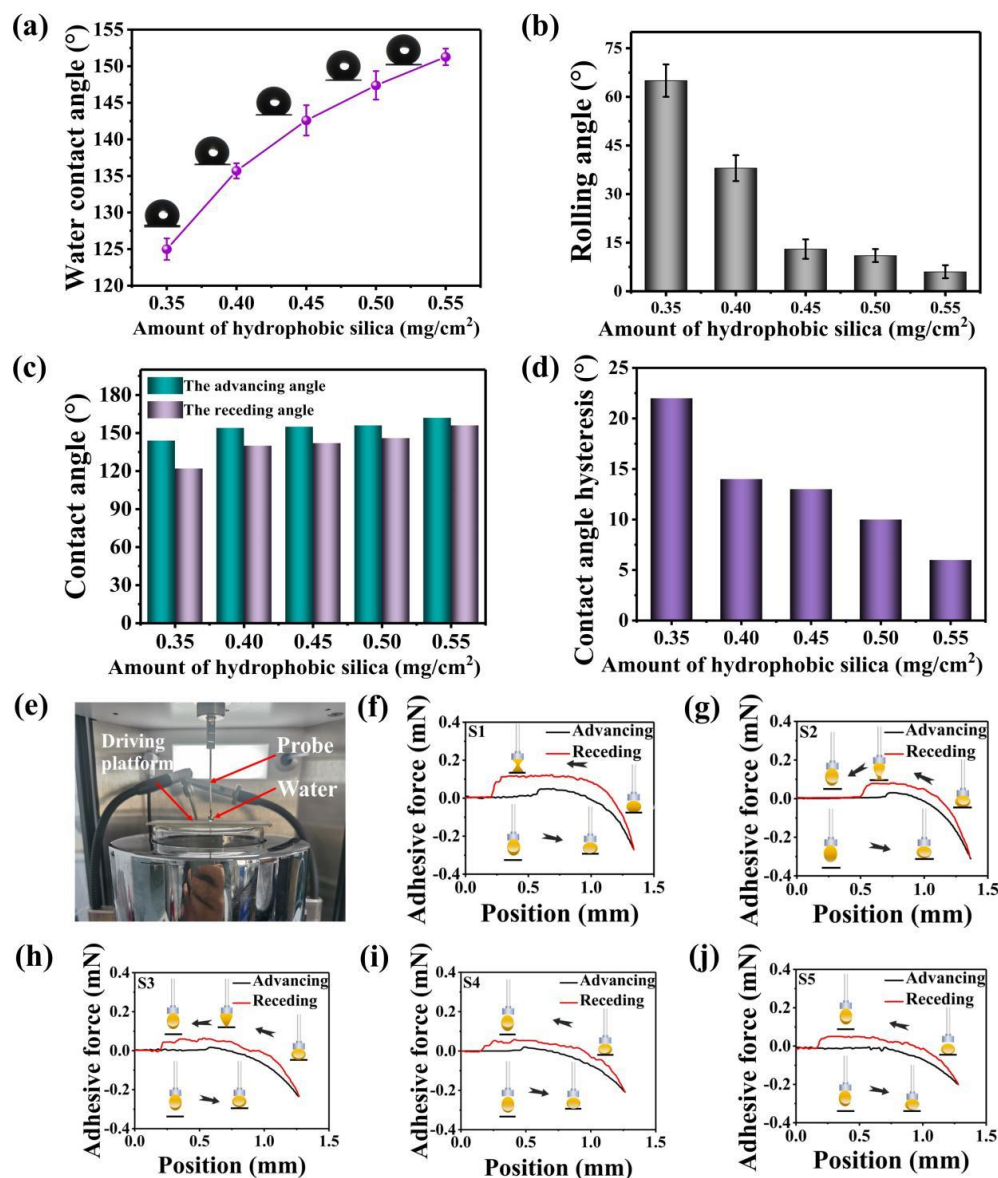
Figure 3 Surface wettability of the SDP sprayed with various amounts of hydrophobic silica: (**a**) water contact angle of droplet; (**b**) rolling angle of a water droplet; (**c**) the advancing angle and receding of a water droplet; (**d**) contact angle hysteresis; (**e**) Real image of the adhesive force testing setup; (**f-j**) Adhesive forces in SDP surface with different amounts of hydrophobic silica (S1:0.35 mg/cm², S2:0.4 mg/cm², S3:0.45 mg/cm², S4:0.5 mg/cm², S5:0.55 mg/cm²).

Fig. 4 (a) shows the real target of the SDP loaded with the optimal spraying content of 0.55 mg/cm², and its surface microstructure is like a rough honeycomb structure (**Fig. 4(b)**). At this point, water droplets are in the Cassie-Baxter state on the superhydrophobic SDP surface, and a layer of air is captured on the superhydrophobic SDP surface, which reduces the contact area between water droplets and SDP[11], resulting in a large contact angle, small contact angle hysteresis and small adhesive force, and small resistance force of droplet movement on the superhydrophobic silica coating surface of thickness of 38.6 μm (**Fig. 4(c)**). SEM-EDS mapping showed

that the expected elements C, O, F, and Si are evenly distributed on the SDP surface (**Fig. 4 (d)**), whose contents are 12.9 wt%, 53.45 wt%, 1.11 wt%, and 33.26 wt%, respectively. XPS photoelectron spectroscopy demonstrates that the characteristic peaks of C1s, F1s, O1s, and Si2p are at ~284.58, ~687.98, ~532.68, and ~103.38 eV, respectively (**Fig. 4(e)**), and its corresponding peak diagram of C-C (284.9 eV), C-F (291.6 eV), and C-Si2P (283.9 eV) (**Fig. 4(f)**), showing that the C-F groups of low surface energy endow the SDP surface with superhydrophobic properties[14].
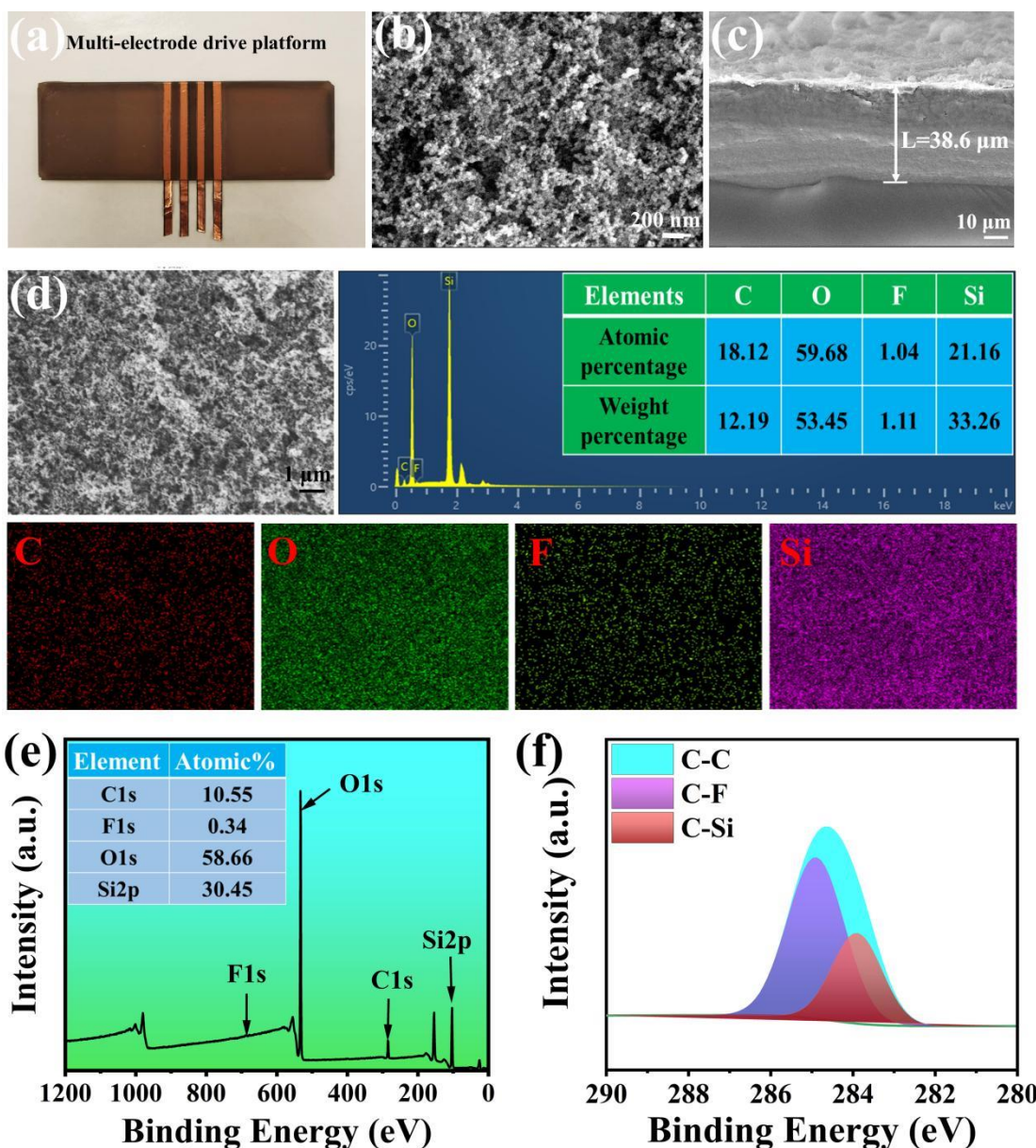
Figure 4 (**a**) Real image of SDP with multi-electrodes; (**b-c**) SEM image of the front and section views of SDP; (**d**) SEM-EDS mapping of SDP surface; (**e**) XPS full spectrum of SDP surface; (**f**) High-solution C1s XPS spectra.

3.3 Water droplets' motion driven by two-electrode SDP

Fig. 5(a) and **(b)** show the real object and its model of TNDDS comprising TENG and SDP with two electrodes, respectively. Since the size and distribution of the electrodes are also crucial for driving charged droplets, the influence of the two factors on the driving critical droplet volume is further examined. As illustrated in Fig. 5(c), while electrode width (W) is fixed at 1 mm, the electrode distance (D) increases gradually from 1 to 3 mm, the V_{min} increases from 3 to 13 μL, and the V_{max} increases from 27 to 121 μL. As illustrated in **Fig. 5(d)**, while D is fixed at 1 mm as W increases from 1 to 3 mm, the V_{min} increases from 3 to 18 μL, and the V_{max} increases from 27 to 140 μL. The results showed that the critical volume of driving water droplets gradually increases with the increase in electrode distance and electrode width, the reason is that the forward motion of a water droplet on SDP is affected by the electrostatic force and friction force. If a larger droplet is driven on the SDP, more positive charges are carried on it, so a larger electrostatic force is exerted on it. Meanwhile, a larger friction force is exerted on it due to its larger volume, so there is a maximum critical volume. Conversely, there also exists a minimum critical volume[49].

The process (i-iii) of **Fig. 5(e)** shows the force analysis of driving water droplets by a TENG. In process i, the water droplet is extruded through a polypropylene tube and placed statically on the surface of the SDP. Positive charges are generated in the water droplets after being rubbed through the inner wall of the polypropylene tube or rubbed against the air [50-53]. Kapton film and aluminum foil as two dielectric materials experience a sliding mode, Kapton film goes on sliding friction back and forth on the surface of two aluminum foils; the two dielectric materials' surfaces are charged because
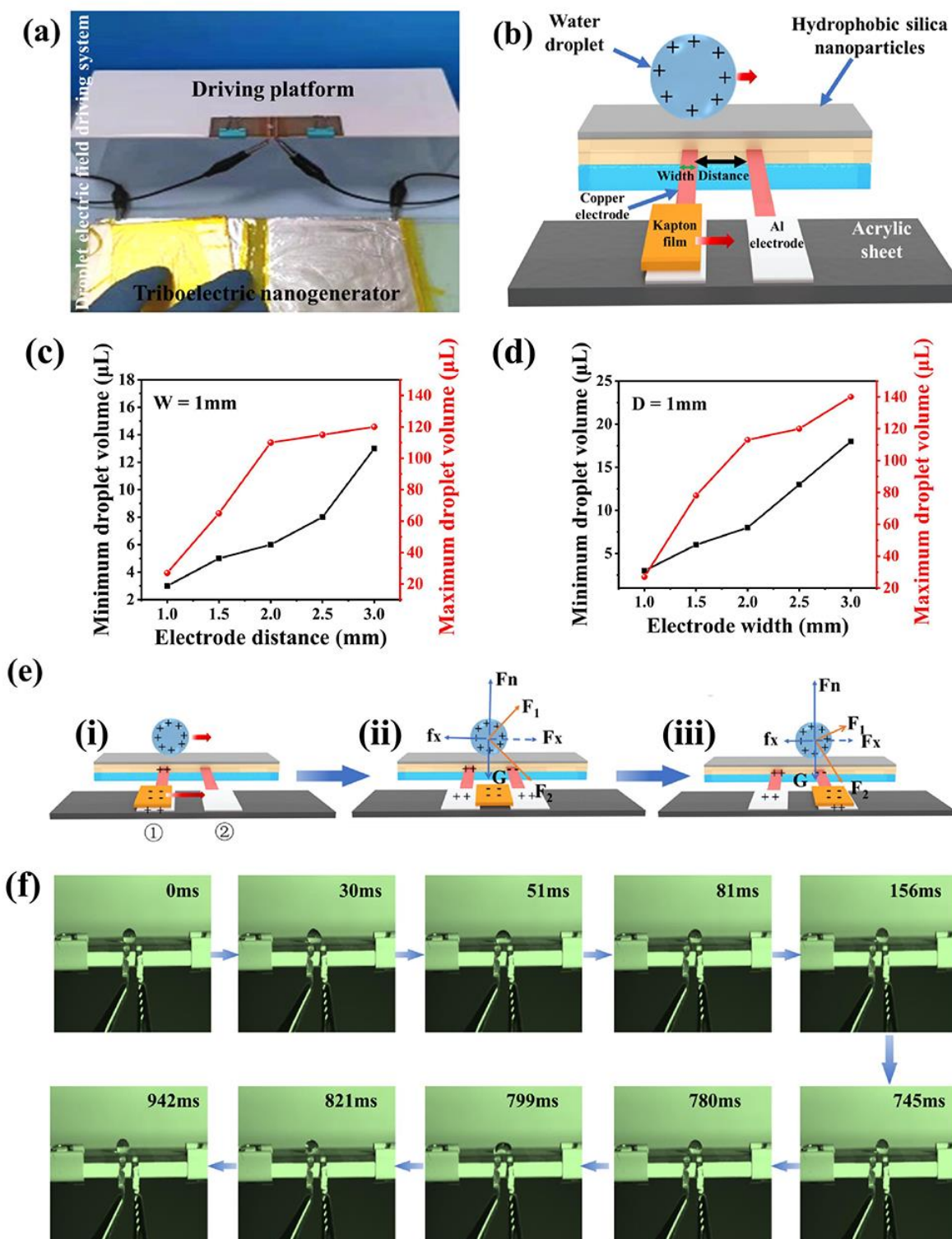
Figure 5 (**a**) Real image of TNDDS comprising TENG and SDP with two electrodes; (**b**) Schematic of the TNDDS model with two electrodes; (**c**) Relation of driving minimum droplet volume (V_{min}) and maximum droplet volume (V_{max}) with electrode distance (D) on the two-electrodes platform (electrode width, W = 1 mm); (**d**) Relation of driving V_{min} and V_{max} with W on the two-electrodes platform (D = 1 mm); (**e**) Force analysis of driving droplet motion process (i-iii) with two electrodes; (**f**) High-definition image of driving droplet motion progress on SDP.

of their triboelectric effect. Kapton film is prone to accept electrons due to its low conductivity, aluminum foils are prone to emit electrons due to their high conductivity, so Kapton film is endowed with negative charges, and aluminum foils are endowed with positive charges [54]. The negative charges on the surface of Kapton film are equal to the sum of the positive charges on the surfaces of the first and second aluminum foils. The accumulated negative charges on the Kapton film surface will increase with constant friction while moving to the first aluminum foil surface again, the total negative charges of Kapton film are higher than the first aluminum foil's total positive charges so that partial negative charges transmit to the first driving electrode connecting to the aluminum foil; however, the first positively charged aluminum foil will conduct positive charge to the first driving electrode to endow it with a positive charge when the Kapton film leaves the first aluminum foil; next, while Kapton film moving to the second aluminum foil, partial negative charges transmit to the second driving electrode connecting to the second aluminum foil, at this time, an electric field is generated between the first positive driving and second negative driving electrodes, it starts to drive the positively charged droplet from the side of the first electrode to the side of the second electrode. The motion process of water droplet being driven back and forth by the TENG with two electrodes was recorded in **Video 1** (ESM). As illustrated in **Fig. 5e(ii)**, the driving force comes from the resultant force exerting on the droplet under the electric field[35]. Horizontally, the positively charged droplet is repelled by the repulsive force (F_1) of the first positively driven electrode and is pulled by an attractive force (F_2) of the second negatively charged driving electrode. Vertically, the friction resistance F_f on SDP when the charged droplet moves forward and the vertical directional gravity (G) and supporting forces (F_n). Since the distance between the droplet and two driving electrodes is constantly changing, the direction and magnitude of the droplet subject to their repulsive and attractive forces are also constantly changing when the droplet moves from the first driving electrode (i) to the second driving electrode (iii). The water droplet can be driven forward as long as the resultant force of F_1 and F_2 in the horizontal direction is greater than the friction force. **Fig. 5(f)** shows the directional transportation process of the water droplet being driven to and fro, as it was captured by a high-speed camera of 1000 frames /S. The water droplet could be driven from the first to the second driving electrode in 156 ms when the Kapton film moves from the first to the second aluminum foil. The water droplet was synchronously

driven from the second electrode to the first electrode in 197 ms after pausing for some time, during which the Kapton film was returned from the second to the first aluminum foil.

3.4 Water droplets's motion is driven by a multi-electrode platform

Theoretically, the number of driving electrodes is appropriately increased, and the movement distance of water droplets can be increased. **Figs. 6(a)** and **6(d)** show a photograph of the TNDDS with four driving electrodes and its model schematic, respectively. As illustrated in **Fig. 6 (b)**, when D is fixed at 1 mm, as W increases from 1 mm to 3 mm, V_{min} driven by the TENG increases from 24 μL to 55 μL, and the V_{max} gradually increases from 90 μL to 286 μL. As illustrated in **Fig. 6(c)**, when D = 2 mm, with the increase in W, the V_{min} reached up to 54, 63, 68, 85, and 103 μL, and the V_{max} reached up to 140, 146, 183, 230, and 295 μL, respectively. As theelectrode distance gradually increases from 1 mm to 3 mm (W = 1 mm), the V_{min} increases from 24 μL to 66 μL, and the V_{max} increases from 90 μL to 150 μL, as illustrated in **Fig. 6(e)**. As illustrated in **Fig. 6(f)**, when the electrodes distance increases from 1 mm to 3 mm (W = 2 mm), the V_{min} increases from 30 μL to 125 μL, and the V_{max} increases from 155 μL to 234 μL. The results also showed that the critical droplet volume increases with the increase in electrode distance when performing multiple driving electrodes. The underlying reason is similar to that of the two electrodes. The motion process of water droplet being driven back and forth by the TENG with four electrodes was recorded in **Video 2** (ESM). **Fig. 6 (g)** shows the force analysis of driving water droplets on the surface of SDP. As aforementioned above, Kapton film was endowed with negative charges after Kapton film going on sliding friction back and forth on the surface of four aluminum foils, and aluminum foils were endowed with positive charges, the negative charges on the Kapton film surface are equal to the sum of the positive charges on the surfaces of the four aluminum foils [(i) in **Fig. 6(g)**]. Electric field is generated between the first positive driving electrode and second negative driving electrode when the Kapton film leaves the first aluminum foil and moves to the second aluminum foil, it starts to drive the positively charged droplets from the side of first electrode to the side of second electrode, a complex electric field of four parallel driving electrodes acts on the charged droplet, the resultant force Fx (F_1, F_2, F_3, and F_4) exerted on the droplet by the four electrodes are illustrated in (ii) of the **Fig. 6(g)**; the Fx in the horizontal direction is greater than the friction force Fx, so that the charged water droplet can be driven forward; the forces

generated by the four electrodes changes from i to iv of **Fig. 6(g)** as the charged droplet moves forward; the directional transportation process of the water droplet being driven to and fro was recorded by a high-speed camera of 1000 frames /S, as shown in **Fig. 6(h)**, while the Kapton film moved from the first

to the four aluminum foil, the water droplet was driven from the first to the four driving electrode in 698 ms; while the Kapton film was returned from the four to the first aluminum foil, the water droplet was synchronously driven back to the first electrode in 1727 ms.
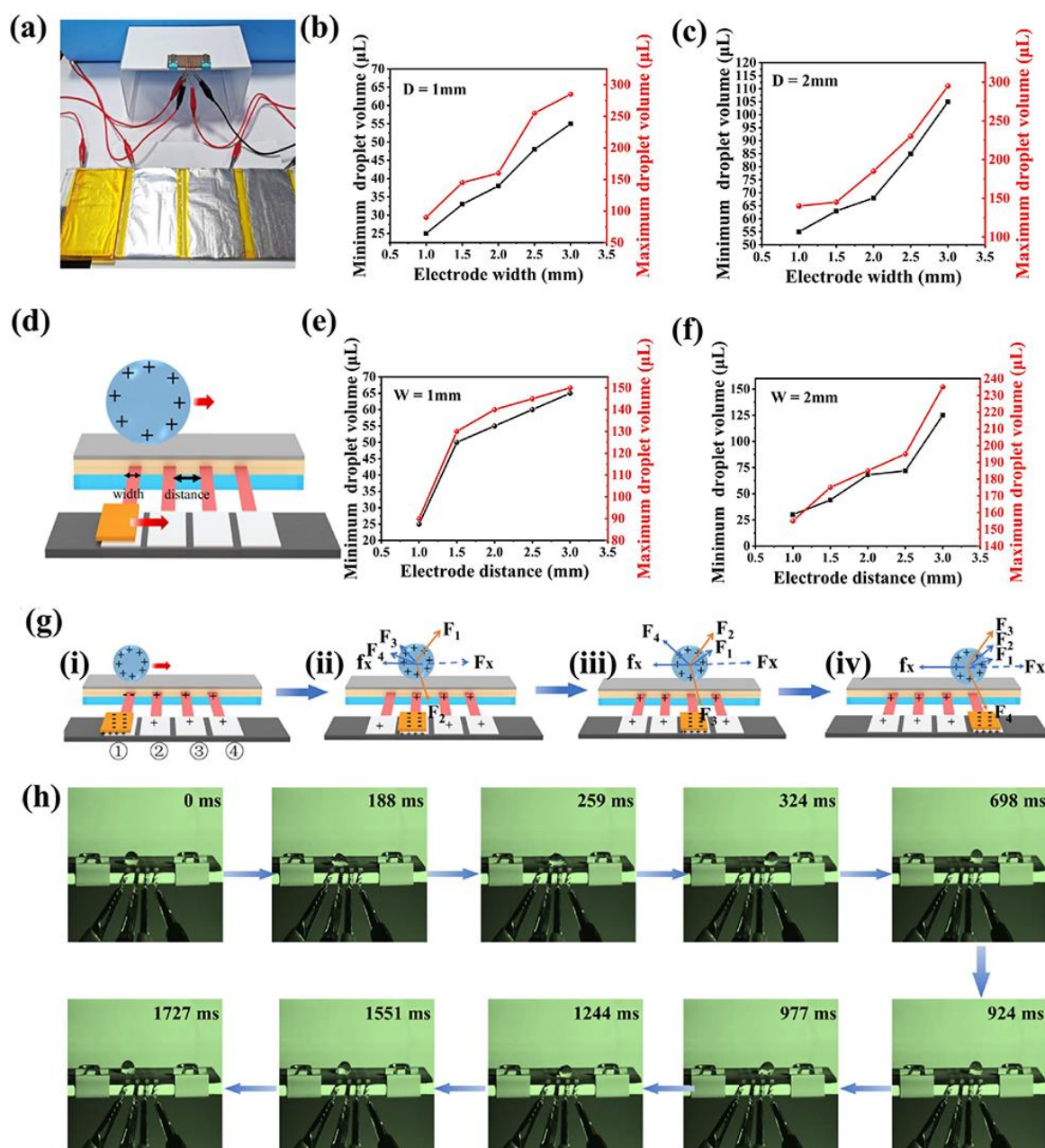

Figure 6 (**a**) Real image of TNDDS comprising TENG and SDP with multiple electrodes; (**b**) Relation of driving V_{min} and V_{max} with W on the four-electrodes platform (D = 1 mm); (**c**) Relation of driving V_{min} and V_{max} with W on the four-electrode platform (D = 2 mm); (**d**) Schematic of TNDDS model with four electrodes; (**e**) Relation of driving V_{min} and V_{max} with D on the four-electrodes platform (W = 1 mm); (**f**) Relation of driving V_{min} and V_{max} with d on the four-electrodes platform (W = 2 mm); (**g**) Force analysis of driving droplet motion process (i-iv) on SDP; (**h**) High-definition camera picture of the droplet motion process on SDP.

3.5 Antibacterial rate of Ag NPs

The Ag NPs were synthesized using the chemical reduction approach, the real physical image of Ag NPs solution and its characterizations was shown in **Figure S3** in the ESM. The

effect of Ag NPs concentration on bactericidal activity against *S.aureus* and *E. coli* was investigated to select an appropriate concentration of Ag NPs solution as a fungicide to kill bacteria on SDP. **Fig. 7(a)** shows that the bactericidal activity is

gradually increased with the increasing concentration of Ag NPs. When the concentration of Ag NPs was 1 mg/mL, the antibacterial rate against *S. aureus* and *E. coli* were 99.01% and 99.61%, respectively. The antibacterial rate of Ag NPs against *E. coli* was higher than that against *S. aureus*, which was due to *E. coli* having more thin cell membranes[55, 56]. **Fig. 7(b)** shows the bacterial colonies on the MHB after Ag NPs against *S. aureus* and *E. coli*. The bacteria on the agar surface of the Petri dish gradually decreased as the concentration of Ag NPs increased from 0.2 to 1 mg/mL. Fluorescence microscopy was used to observe the ratio and state of dead and live bacteria, as illustrated in **Fig. 7(c)**, live and dead bacteria were dyed with green and red, respectively, both for *S. aureus* and *E. coli,* and the observed colony number proportion of dead bacteria increased and live bacteria decreased with increasing concentration of Ag NPs. **Fig. 7(d)** elucidates the bactericidal mechanism of Ag NPs. The higher atomic density on the surface of the Ag NPs makes it more active, the positively charged silver ions were slowly released from Ag NPs, and act with the negatively charged bacterial membrane through an electrostatic effect to damage the cell membrane and make the cell matrix dissolve out. Silver ions permeate into the bacteria in the cytoplasm to allow the respiratory chain dehydrogenase inactive, thus inhibiting cell respiration and growth; simultaneously, the Ag NPs can affect parts of protein and lipid phosphate, inducing cell membrane collapse, and eventually resulting in cell decomposition and death[57-60].
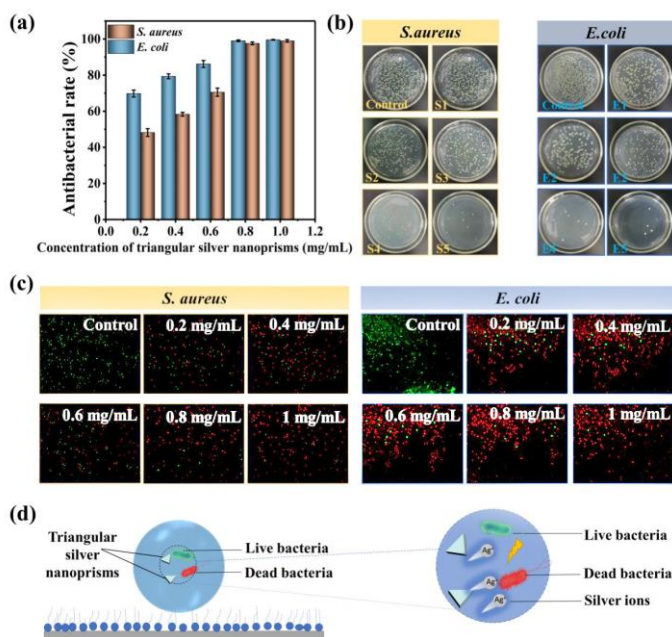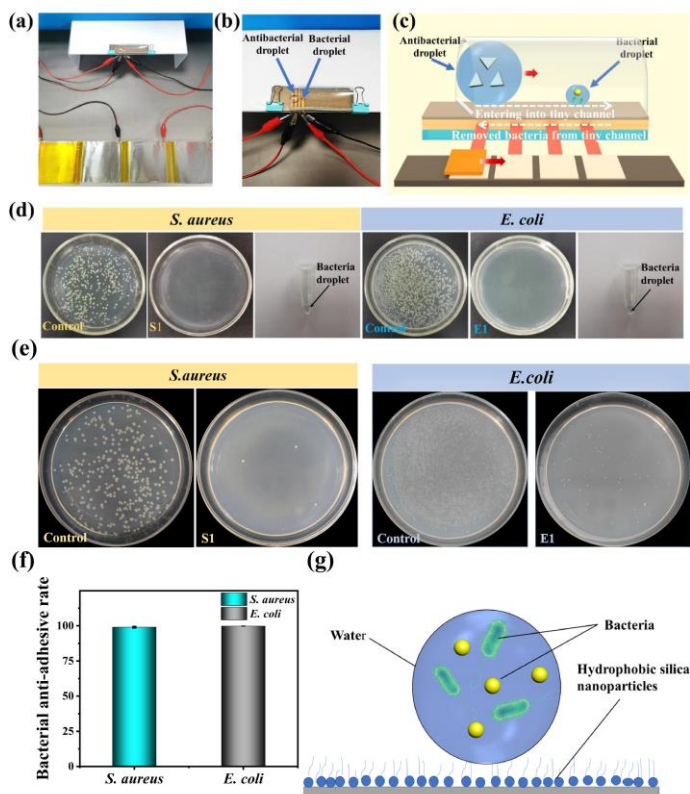
Figure 7 (**a**) Antibacterial rates of Ag NPs with different concentrations (0.2, 0.4, 0.6, 0.8, and 1.0 mg/mL); (**b**) Bacterial colonies on the MHB after Ag NPs with different concentrations (S1: 0.2 mg/mL S2: 0.4 mg/mL, S3:

0.6 mg/mL, S4: 0.8 mg/mL, and S5: 1 mg/mL) against *S. aureus* and *E. coli*; (**c**) Fluorescence microscopy images after the antibacterial test of Ag NPs against *S. aureus* and *E. coli*; (**d**) Bactericidal mechanism model of Ag NP.

3.6 Bacterial removal and killing realized by TNDDS

To simulate the removal of bacteria from the difficult-to-cleanable material surface, 5 μL bacterial droplets were added to the four-electrode SDP in a semi-closed tiny channel (**Fig. 8 a**) in advance, near the left of the fourth electrode, and then 100 μL droplets of 1 mg/mL Ag NPs were dropped on the left of the first electrode (**Fig. 8 b**). Driving by TENG, the droplet of Ag NPs was moved forward to the right direction until it mixed with the bacterial droplet, and then returned reciprocally to the left direction to remove the bacteria (**Fig. 8 c**). The bacterial colonies before and after being killed were counted by the plate counting approach. **Fig. 8(d)** shows that the removed bacteria on SDP were completely killed, and the antibacterial rates of the mixed droplets against *S. aureus* and *E. coli* can reach 100% because of the existing Ag NPs. To measure the removal performance of small bacterial droplets by directional motion, the motion trajectory was eluted with sterile water to evaluate whether the presence of residual adherent bacteria or not. Bacterial colonies were observed on the MHA surface of Petri dishes. Fig. 8(e) shows the presence of many bacterial colonies on the surface of the control (small bacterial droplet) and few bacterial colonies on S1 and E1, indicating few residual adherent bacteria on the motion trajectory of the mixed droplet, its anti-adhesion rates against S. aureus and E. coli can both near 100% [Fig. 8(f)], this was attributed to the superhydrophobicity of the SDP surface. The reason why a superhydrophobic surface is beneficial for reducing bacterial adhesion is that superhydrophobic silica nanoparticles were sprayed on the SDP surface, and silica nanoparticles have long chain hydrophobic groups, so stable nanostructure and low surface energy made the SDP in a Cassie state, as illustrated in **Fig. 8(g)**, just like there exists a stable air mattress at the interface between the superhydrophobic SDP surface and bacterial droplet, making bacterial droplet present a Cassie state on the superhydrophobic SDP surface, which can substantially reduce the contact area of liquid-solid interface, thereby reducing bacterial adhesion[13, 61].

Figure 8 (**a**) Real image of TNDDS with four-electrode SDP in a semi-closed tiny channel; Real image (**b**) and its model (**c**) of bacterial droplet driving and removing application of TNDDS; (**d**) Bacterial colonies (*S. aureus* and *E. coli*) on the MHA before and after Ag NPs droplet mixing with bacteria droplet driven by TENG for bactericidal performance assessment; (**e**) Colonies on the MHB of bacteria (*S. aureus* and *E. coli*) on the motion trajectory eluted by sterile water for bacterial anti-adhesion assessment; (**f**) Bacterial anti-adhesion rates of SDP after performing bacterial droplet driving application; (**g**) Model of bacterial anti-adhesion.

4 Conclusions

In conclusion, different from passive defense strategies, an active bacterial anti-adhesion strategy based on directional driving transportation of bacterial droplets on driving SDP driven by a TENG was proposed. Water or bacterial droplets on a superhydrophobic driving SDP could be driven by manipulating the horizontal periodic reciprocating friction between the Kapton film and the aluminum foil plate of the TNDDS system. The underlying mechanism of driving droplets is that the charged droplets are subjected to the resultant electric force of parallel driving electrodes transmitted with current on the SDP, and the current was generated by TENG triboelectricity. The findings showed that superhydrophobic driving SDP modified with silica nanoparticles in a Cassie state is propitious to droplet driving motion because of its extremely low surface friction resistance; the critical value of driven droplet volume on SDP is closely related to the distributed electrodes' distance and width, and the driving distance of droplets is related to the number of electrodes. TNDDS can also actively drive the charged droplets of prepared bactericidal Ag NPs forward and back to mix with and remove small bacterial droplets on an open SDP or in a tiny semi-enclosed channel. Bacteria could be killed by releasing Ag$^+$ and effectively removed by TNDDS by regulating the motion direction, and no residual adherent bacteria were on their motion trajectory on

SDP with a superb bacterial anti-adhesive rate. Thus, TNDDS was shown to be effective in the removal of bacteria from the difficult-to-cleanable material surface. This approach opens a new avenue for bacterial anti-adhesion.

Acknowledgements

Electronic Supplementary Material: Supplementary material (further details of the rolling process and adhesive forces of water droplets on the SDP surface, and the characterization of Ag NPs; the motion process of the water droplet being driven back and forth by the TENG with two electrodes is recorded in Video 1; the motion process of water droplets being driven back and forth by the TENG on the surface of SDP with four electrodes was recorded in Video 2) is available in the online version of this article at http://dx.doi.org/10.1007/s12274-***-****-* (automatically inserted by the publisher).

References

[1]   Costerton, J. W.;Stewart, P. S.; Greenberg, E. P. Bacterial biofilms: a common cause of persistent infections. *Science* **1999**, *284*, 1318-1322.

[2]   Yang, X.;Hou, J.;Tian, Y.;Zhao, J.;Sun, Q.; Zhou, S. Antibacterial surfaces: Strategies and applications. *Sci. China Technol. Sc.* **2022**,

10.1007/s11431-021-1962-x, 1-11.

[3] Rajasekar, A.;Anandkumar, B.;Maruthamuthu, S.;Ting, Y. P.; Rahman, P. K. Characterization of corrosive bacterial consortia isolated from petroleum-product-transporting pipelines. *Appl. Microbiol. Biotechnol.* **2010**, *85*, 1175-1188.

[4] Khan, M. M.;Ista, L. K.;Lopez, G. P.; Schuler, A. J. Experimental and theoretical examination of surface energy and adhesion of nitrifying and heterotrophic bacteria using self-assembled monolayers. *Environ. Sci. Technol.* **2011**, *45*, 1055-1060.

[5] Tyers, M.; Wright, G. D. Drug combinations: a strategy to extend the life of antibiotics in the 21st century. *Nat. Rev. Microbiol.* **2019**, *17*, 141-155.

[6] Lin, J.;Chen, X.;Chen, C.;Hu, J.;Zhou, C.;Cai, X.;Wang, W.;Zheng, C.;Zhang, P.;Cheng, J.;Guo, Z.; Liu, H. Durably Antibacterial and Bacterially Antiadhesive Cotton Fabrics Coated by Cationic Fluorinated Polymers. *ACS Appl. Mater. Interfaces* **2018**, *10*, 6124-6136.

[7] Wang, Y.;Liu, Z.;Wei, X.;Liu, K.;Wang, J.;Hu, J.; Lin, J. An integrated strategy for achieving oil-in-water separation, removal, and anti-oil/dye/bacteria-fouling. *Chem. Eng. J.* **2021**, *413*.

[8] Fatima, A.;Yasir, S.;Ul-Islam, M.;Kamal, T.;Ahmad, M. W.;Abbas, Y.;Manan, S.;Ullah, M. W.; Yang, G. Ex situ development and characterization of green antibacterial bacterial cellulose-based composites for potential biomedical applications. *Adv. Compos. Hybrid Mater.* **2021**, *5*, 307-321.

[9] Zhou, K.;Wang, M.;Zhou, Y.;Sun, M.;Xie, Y.; Yu, D.-G. Comparisons of antibacterial performances between electrospun polymer@drug nanohybrids with drug-polymer nanocomposites. *Adv. Compos. Hybrid Mater.* **2022**, *5*, 907-919.

[10] Feng, L.;Li, S.;Li, Y.;Li, H.;Zhang, L.;Zhai, J.;Song, Y.;Liu, B.;Jiang, L.; Zhu, D. Super-Hydrophobic Surfaces: From Natural to Artificial. *Adv. Mater.* **2002**, *14*, 1857-1860.

[11] Barthlott, W.; Neinhuis, C. Purity of the sacred lotus, or escape from contamination in biological surfaces. *Planta* **1997**, *202*, 1-8.

[12] Geyer, F.;D'Acunzi, M.;Yang, C.-Y.;Müller, M.;Baumli, P.;Kaltbeitzel, A.;Mailänder, V.;Encinas, N.;Vollmer, D.; Butt, H.-J. How to Coat the Inside of Narrow and Long Tubes with a Super-Liquid-Repellent Layer-A Promising Candidate for Antibacterial Catheters. *Adv. Mater.* **2019**, *31*.

[13] Jiang, R.;Hao, L.;Song, L.;Tian, L.;Fan, Y.;Zhao, J.;Liu, C.;Ming, W.; Ren, L. Lotus-leaf-inspired hierarchical structured surface with non-fouling and mechanical bactericidal performances. *Chem. Eng. J.* **2020**, *398*.

[14] Lin, J.;Cai, X.;Liu, Z.;Liu, N.;Xie, M.;Zhou, B.;Wang, H.; Guo, Z. Anti-liquid-Interfering and Bacterially Antiadhesive Strategy for Highly Stretchable and Ultrasensitive Strain Sensors Based on Cassie-Baxter Wetting State. *Adv. Funct. Mater.* **2020**, *30*.

[15] Lin, J.;Hu, J.;Wang, W.;Liu, K.;Zhou, C.;Liu, Z.;Kong, S.;Lin, S.;Deng, Y.; Guo, Z. Thermo and light-responsive strategies of smart titanium-containing composite material surface for enhancing bacterially anti-adhesive property. *Chem. Eng. J.* **2021**, *407*.

[16] Lin, J.;Wang, Y.;Wei, X.;Kong, S.;Liu, Z.;Liu, J.;Zhang, F.;Lin, S.;Ji, B.;Zhou, Z.; Guo, Z. Controllable antibacterial and bacterially anti-adhesive surface fabricated by a bio-inspired beetle-like macromolecule. *Int. J. Biol. Macromol.* **2020**, *157*, 553-560.

[17] Gui, L.;Lin, J.;Liu, J.;Zuo, J.;Wang, Q.;Jiang, W.;Feng, T.;Li, S.;Wang, S.; Liu, Z. Difference and association of antibacterial and bacterial anti-adhesive performances between smart Ag/AgCl/TiO$_2$ composite surfaces with switchable wettability. *Chem. Eng. J.* **2022**, *431*.

[18] Hu, J.;Lin, J.;Zhang, Y.;Lin, Z.;Qiao, Z.;Liu, Z.;Yang, W.;Liu, X.;Dong, M.; Guo, Z. A new anti-biofilm strategy of enabling arbitrary surfaces of materials and devices with robust bacterial anti-adhesion via a spraying modified microsphere method. *J. Mater. Chem. A* **2019**, *7*, 26039-26052.

[19] Wang, J.;Wu, H.;Yang, Y.;Yan, R.;Zhao, Y.;Wang, Y.;Chen, A.;Shao, S.;Jiang, P.; Li, Y. Q. Bacterial species-identifiable magnetic nanosystems for early sepsis diagnosis and extracorporeal photodynamic blood disinfection. *Nanoscale* **2017**, *10*, 132-141.

[20] Jiang, S.; Cao, Z. Ultralow-fouling, functionalizable, and hydrolyzable zwitterionic materials and their derivatives for biological applications. *Adv. Mater.* **2010**, *22*, 920-932.

[21] Zhao, W.;Yang, J.;Guo, H.;Xu, T.;Li, Q.;Wen, C.;Sui, X.;Lin, C.;Zhang, J.; Zhang, L. Slime-resistant marine anti-biofouling coating with PVP-based copolymer in PDMS matrix. *Chem. Eng. Sci.* **2019**, *207*, 790-798.

[22] Mei, Y.;Yu, K.;Lo, J. C. Y.;Takeuchi, L. E.;Hadjesfandiari, N.;Yazdani-Ahmadabadi, H.;Brooks, D. E.;Lange, D.; Kizhakkedathu, J. N. Polymer-Nanoparticle Interaction as a Design Principle in the Development of a Durable Ultrathin Universal Binary Antibiofilm Coating with Long-Term Activity. *ACS Nano* **2018**, *12*, 11881-11891.

[23] Zhang, D.;Wang, L.;Qian, H.; Li, X. Superhydrophobic surfaces for corrosion protection: a review of recent progresses and future directions. *J. Coat. Technol. Res.* **2015**, *13*, 11-29.

[24] Fan, F.-R.;Tian, Z.-Q.; Lin Wang, Z. Flexible triboelectric generator. *Nano Energy* **2012**, *1*, 328-334.

[25] Wang, S.;Mu, X.;Wang, X.;Gu, A. Y.;Wang, Z. L.; Yang, Y. Elasto-Aerodynamics-Driven Triboelectric Nanogenerator for Scavenging Air-Flow Energy. *ACS Nano* **2015**, *9*, 9554-9563.

[26] Zhang, Y.;Zeng, Q.;Wu, Y.;Wu, J.;Yuan, S.;Tan, D.;Hu, C.; Wang, X. An Ultra-Durable Windmill-Like Hybrid Nanogenerator for Steady and Efficient Harvesting of Low-Speed Wind Energy. *Nanomicro Lett.* **2020**, *12*, 175.

[27] Chen, J.;Zhu, G.;Yang, W.;Jing, Q.;Bai, P.;Yang, Y.;Hou, T. C.; Wang, Z. L. Harmonic-resonator-based triboelectric nanogenerator as a sustainable power source and a self-powered active vibration sensor. *Adv. Mater.* **2013**, *25*, 6094-6099.

[28] Yang, W.;Chen, J.;Zhu, G.;Wen, X.;Bai, P.;Su, Y.;Lin, Y.; Wang, Z. Harvesting vibration energy by a triple-cantilever based triboelectric nanogenerator. *Nano Res.* **2013**, *6*, 880-886.

[29] Xu, M.;Zhao, T.;Wang, C.;Zhang, S. L.;Li, Z.;Pan, X.; Wang, Z. L. High Power Density Tower-like Triboelectric Nanogenerator for Harvesting Arbitrary Directional Water Wave Energy. *ACS Nano* **2019**, *13*, 1932-1939.

[30] Wang, Y.;Huang, T.;Gao, Q.;Li, J.;Wen, J.;Wang, Z. L.; Cheng, T. High-voltage output triboelectric nanogenerator with DC/AC optimal combination method. *Nano Res.* **2021**, *15*, 3239-3245.

[31] Yang, W.;Chen, J.;Jing, Q.;Yang, J.;Wen, X.;Su, Y.;Zhu, G.;Bai, P.; Wang, Z. L. 3D Stack Integrated Triboelectric Nanogenerator for Harvesting Vibration Energy. *Adv. Funct. Mater.* **2014**, *24*, 4090-4096.

[32] Wang, S.;Lin, L.; Wang, Z. L. Triboelectric nanogenerators as self-powered active sensors. *Nano Energy* **2015**, *11*, 436-462.

[33] Tan, D.;Zeng, Q.;Wang, X.;Yuan, S.;Luo, Y.;Zhang, X.;Tan, L.;Hu, C.; Liu, G. Anti-Overturning Fully Symmetrical Triboelectric Nanogenerator Based on an Elliptic Cylindrical Structure for All-Weather Blue Energy Harvesting. *Nanomicro Lett.* **2022**, *14*, 124.

[34] Wang, D.;Zhang, D.;Li, P.;Yang, Z.;Mi, Q.; Yu, L. Electrospinning of Flexible Poly(vinyl alcohol)/MXene Nanofiber-Based Humidity Sensor Self-Powered by Monolayer Molybdenum Diselenide Piezoelectric Nanogenerator. *Nanomicro Lett.* **2021**, *13*, 57.

[35] Yang, X.;Xu, L.;Lin, P.;Zhong, W.;Bai, Y.;Luo, J.;Chen, J.; Wang, Z. L. Macroscopic self-assembly network of encapsulated high-performance triboelectric nanogenerators for water wave energy harvesting. *Nano Energy* **2019**, *60*, 404-412.

[36] Chen, X.;Wu, Y.;Yu, A.;Xu, L.;Zheng, L.;Liu, Y.;Li, H.; Lin Wang, Z. Self-powered modulation of elastomeric optical grating by using triboelectric nanogenerator. *Nano Energy* **2017**, *38*, 91-100.

[37] Chen, X.;Pu, X.;Jiang, T.;Yu, A.;Xu, L.; Wang, Z. L. Tunable Optical Modulator by Coupling a Triboelectric Nanogenerator and a Dielectric Elastomer. *Adv. Funct. Mater.* **2017**, *27*.

[38] Wen, Z.;Shen, Q.; Sun, X. Nanogenerators for Self-Powered Gas Sensing. *Nanomicro Lett.* **2017**, *9*, 45.

[39] Zhang, K.; Yang, Y. Linear-grating hybridized electromagnetic-triboelectric nanogenerator for sustainably powering portable electronics. *Nano Res.* **2016**, *9*, 974-984.

[40] Gao, Y.;Liu, G.;Bu, T.;Liu, Y.;Qi, Y.;Xie, Y.;Xu, S.;Deng, W.;Yang, W.; Zhang, C. MXene based mechanically and electrically enhanced film for triboelectric nanogenerator. *Nano Res.* **2021**, *14*, 4833-4840.

[41] Ma, M.;Kang, Z.;Liao, Q.;Zhang, Q.;Gao, F.;Zhao, X.;Zhang, Z.; Zhang, Y. Development, applications, and future directions of triboelectric nanogenerators. *Nano Res.* **2018**, *11*, 2951-2969.

[42] Chen, X.;Jiang, T.;Yao, Y.;Xu, L.;Zhao, Z.; Wang, Z. L. Stimulating Acrylic Elastomers by a Triboelectric Nanogenerator - Toward

[43] Self-Powered Electronic Skin and Artificial Muscle. *Adv. Funct. Mater.* **2016**, *26*, 4906-4913.

[43] Zhang, Q.;Li, N.;Goebl, J.;Lu, Z.; Yin, Y. A systematic study of the synthesis of silver nanoplates: is citrate a "magic" reagent? *J. Am. Chem. Soc.* **2011**, *133*, 18931-18939.

[44] Nie, J.;Ren, Z.;Shao, J.;Deng, C.;Xu, L.;Chen, X.;Li, M.; Wang, Z. L. Self-Powered Microfluidic Transport System Based on Triboelectric Nanogenerator and Electrowetting Technique. *ACS Nano* **2018**, *12*, 1491-1499.

[45] Li, X.;Zhao, L.;Yu, J.;Liu, X.;Zhang, X.;Liu, H.; Zhou, W. Water Splitting: From Electrode to Green Energy System. *Nanomicro Lett.* **2020**, *12*, 131.

[46] Chen, Y.;Lin, J.;Mersal, G. A. M.;Zuo, J.;Li, J.;Wang, Q.;Feng, Y.;Liu, J.;Liu, Z.;Wang, B.;Xu, B. B.; Guo, Z. "Several birds with one stone" strategy of pH/thermoresponsive flame-retardant/photothermal bactericidal oil-absorbing material for recovering complex spilled oil. *J. Mater. Sci. Technol.* **2022**, *128*, 82-97.

[47] Hu, J.;Gui, L.;Zhu, M.;Liu, K.;Chen, Y.;Wang, X.; Lin, J. Smart Janus membrane for on-demand separation of oil, bacteria, dye, and metal ions from complex wastewater. *Chem. Eng. Sci.* **2022**, *253*.

[48] Liu, J.;Zheng, N.;Li, Z.;Liu, Z.;Wang, G.;Gui, L.; Lin, J. Fast self-healing and antifouling polyurethane/fluorinated polysiloxane-microcapsules-silica composite material. *Adv. Compos. Hybrid Mater.* **2022**, 10.1007/s42114-022-00515-1.

[49] Yu, J.;Wei, X.;Guo, Y.;Zhang, Z.;Rui, P.;Zhao, Y.;Zhang, W.;Shi, S.; Wang, P. Self-powered droplet manipulation system for microfluidics based on triboelectric nanogenerator harvesting rotary energy. *Lab Chip* **2021**, *21*, 284-295.

[50] Nauruzbayeva, J.;Sun, Z.;Gallo, A., Jr.;Ibrahim, M.;Santamarina, J. C.; Mishra, H. Electrification at water-hydrophobe interfaces. *Nat. Commun.* **2020**, *11*, 5285.

[51] Nie, J.;Ren, Z.;Xu, L.;Lin, S.;Zhan, F.;Chen, X.; Wang, Z. L. Probing Contact-Electrification-Induced Electron and Ion Transfers at a Liquid-Solid Interface. *Adv. Mater.* **2020**, *32*, e1905696.

[52] Choi, D.;Lee, H.;Im, D. J.;Kang, I. S.;Lim, G.;Kim, D. S.; Kang, K. H. Spontaneous electrical charging of droplets by conventional pipetting. *Sci. Rep.* **2013**, *3*, 2037.

[53] Geyer, F.;D'Acunzi, M.;Yang, C. Y.;Muller, M.;Baumli, P.;Kaltbeitzel, A.;Mailander, V.;Encinas, N.;Vollmer, D.; Butt, H. J. How to Coat the Inside of Narrow and Long Tubes with a Super-Liquid-Repellent Layer-A Promising Candidate for Antibacterial Catheters. *Adv. Mater.* **2019**, *31*, e1801324.

[54] Wang, Z. L. Triboelectric nanogenerators as new energy technology and self-powered sensors - principles, problems and perspectives. *Faraday Discuss.* **2014**, *176*, 447-458.

[55] Njagi, J.;Chernov, M. M.;Leiter, J. C.; Andreescu, S. Amperometric detection of dopamine in vivo with an enzyme based carbon fiber

microbiosensor. *Anal. Chem.* **2010**, *82*, 989-996.

[56] Fortunati, E.;Mattioli, S.;Visai, L.;Imbriani, M.;Fierro, J. L.;Kenny, J. M.; Armentano, I. Combined effects of Ag nanoparticles and oxygen plasma treatment on PLGA morphological, chemical, and antibacterial properties. *Biomacromolecules* **2013**, *14*, 626-636.

[57] Panthi, G.;Ranjit, R.;Khadka, S.;Gyawali, K. R.;Kim, H.-Y.; Park, M. Characterization and antibacterial activity of rice grain-shaped ZnS nanoparticles immobilized inside the polymer electrospun nanofibers. *Adv. Compos. Hybrid Mater.* **2020**, *3*, 8-15.

[58] Singh, M.;Bajaj, N. K.;Bhardwaj, A.;Singh, P.;Kumar, P.; Sharma, J.

Study of photocatalytic and antibacterial activities of graphene oxide nanosheets. *Adv. Compos. Hybrid Mater.* **2018**, *1*, 759-765.

[59] Li, W. R.;Xie, X. B.;Shi, Q. S.;Zeng, H. Y.;Ou-Yang, Y. S.; Chen, Y. B. Antibacterial activity and mechanism of silver nanoparticles on Escherichia coli. *Appl. Microbiol. Biotechnol.* **2010**, *85*, 1115-1122.

[60] Sondi, I.; Salopek-Sondi, B. Silver nanoparticles as antimicrobial agent: a case study on E. coli as a model for Gram-negative bacteria. *J. Colloid Interface Sci.* **2004**, *275*, 177-182.

[61] Marmur, A. Super-hydrophobicity fundamentals: implications to biofouling prevention. *Biofouling* **2006**, *22*, 107-115.